

Theoretical model of the formation of cold-rolling textures: texture stability criteria and application to cubic metals

A. SPOLIDOR, C. GOUX*

*Manoir Industres, Pitres, France, * Ecole Nationale Supérieure des Mines de Saint-Etienne, France*

From observations made on pole figures typical of body-centred and face-centred cubic metals, and on the basis of calculations correlated with the energetic concept of maximum plastic work principle, three stability criteria are defined which allow the equilibrium positions of a crystal to be determined. A verification of the validity of these three criteria is then carried out by calculating the orientations of the different possible stable textures. Because the results agree well with experiments, they validate the different assumptions retained.

1. Introduction

Many papers have been published to explain the formation of cold-rolling textures, in particular, Sachs [1] whose model imposed the stress repartition in each crystal of the aggregate during deformation, and Boas and Schmid [2] who assigned the method of deformation of the given crystal; the advantage of this second model in comparison with the first is that an identical deformation for all crystals would lead to the intercrystalline cohesion of the metal.

Other works [3–15] followed these initial investigations, especially concerning cold rolling of face-centred cubic metals which produces three different textures according to the type of metal considered: copper-, α -brass- and cerium-type textures. The authors tried to connect the appearance of these textures with physical phenomena significant to the way in which the face-centred cubic metal was deformed: formation of stacking faults [16], interactions between dislocations [17], cross slip [12, 18], twinning [19–21, 13], glide on planes $\{001\}$ [10, 22–29]. These different interpretations nevertheless do not appear entirely satisfactory because of the lack of an inclusive theory of cold rolling providing a synthesis of experimental results observed on both body-centred and face-centred cubic metals.

The purpose of the present study was precisely to try to build a similar theory which could explain the appearance of the different textures noticed when body-centred and face-centred cubic metal cold rolling occurs.

2. Experimental basis of the theory

Observation of cold-rolled body-centred cubic metal pole figures $\{110\}$ (Fig. 1a) and face-centred cubic metal pole figures $\{111\}$ (Fig. 1b) shows that maximum densities of X-ray reflections appear for reflection planes having their normal direction in a plane

π (area A and B). This plane, π , is defined by the normal direction of the plane of the rolled sheet and by the rolling direction; it was consequently orthogonal to the roller axis during cold rolling (Fig. 2).

These planes $\{110\}$ and $\{111\}$, which are reflection planes for X-rays, are also glide planes for body-centred and face-centred cubic metals, respectively. This leads us to assume that during cold rolling and crystalline rotations in the metal, glide planes have a tendency to adopt an orientation which puts its normal direction in a plane orthogonal to the roller axis. In the case of the α -brass-type texture, these are glide directions $\langle 110 \rangle$ which go in the plane π (Fig. 3a and b).

The first observation may therefore be inferred.

Observation 1. In the course of cold rolling, some directions normal to glide planes of the metal, as well as glide directions, have a tendency to move into the plane π , defined by the normal direction to the rolled sheet and by the rolling direction; this plane, π , was orthogonal to the roller axis during cold rolling.

On the other hand, calculation of shear stresses on the most loaded slip planes (and therefore probably the most active) of a body-centred cubic system standard stable texture, $\{001\} \langle 110 \rangle$, has revealed that the moduli of these stresses are equal (for slip systems of $\{112\} \langle 111 \rangle$ type). The mathematical expression used for the calculation of these shear stresses has the following form

$$\tau = C[\cos \lambda_c \cos \phi_c - \cos \lambda_t \cos \phi_t] \quad (1)$$

which we shall later justify. The notation used for this expression is defined in Fig. 4.

Similar calculations made on other stable textures of body-centred cubic metals, $\{112\} \langle 110 \rangle$, $\{111\} \langle 112 \rangle$, and of face-centred cubic metals, $\{112\} \langle 111 \rangle$, $\{110\} \langle 112 \rangle$, $\{110\} \langle 001 \rangle$, lead to the same results. So, two further observations may be inferred.

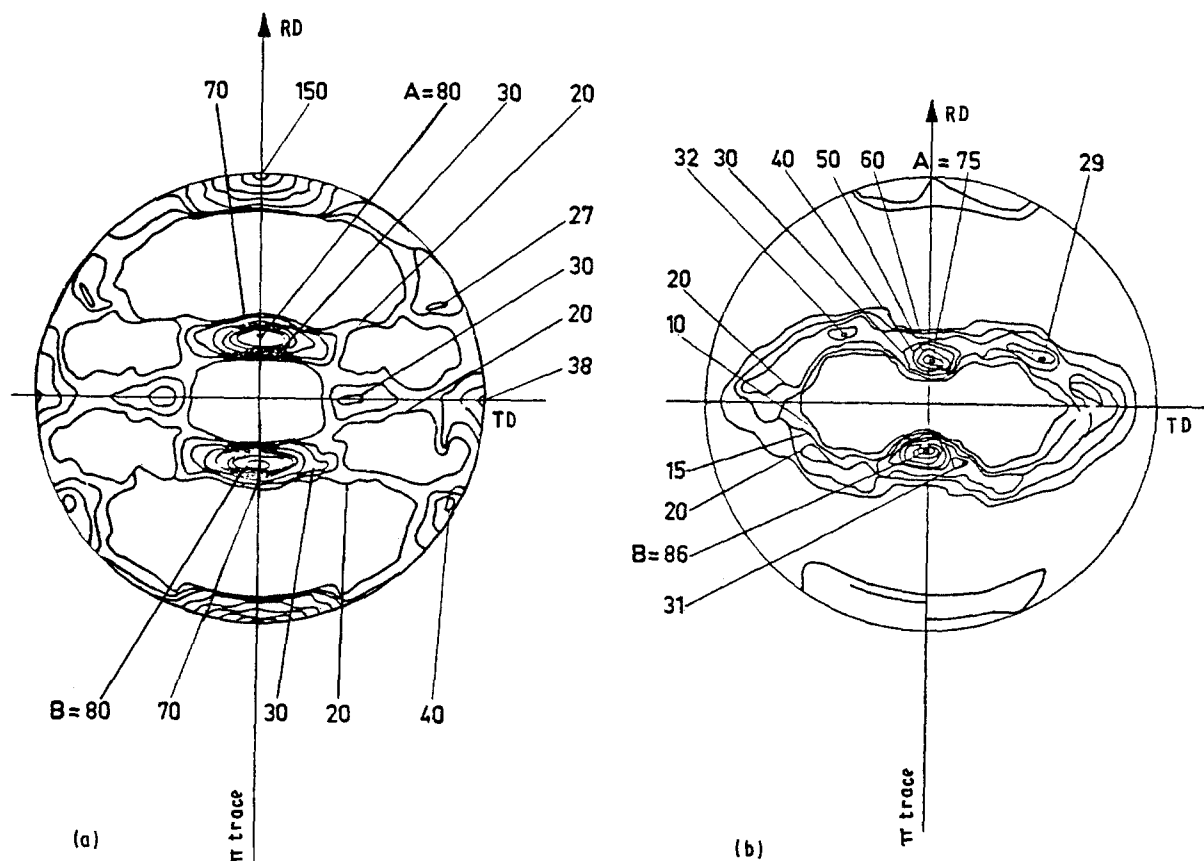


Figure 1 (a) $\{110\}$ pole figure of 90% at 20 °C cold-rolled high purity iron. (b) $\{111\}$ pole figure of 90% at 20 °C cold-rolled OFHC copper.

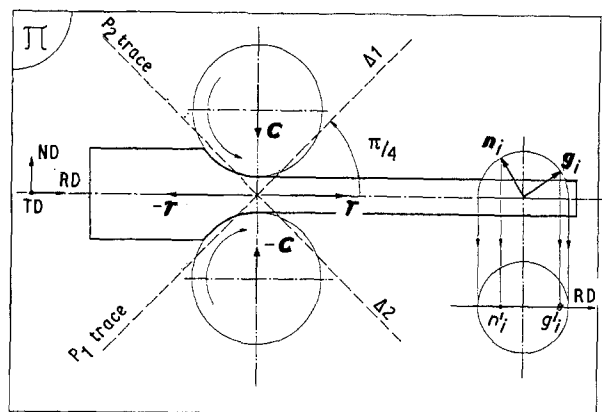


Figure 2 Rolling in biaxial deviatoric stresses C and T . Definition of the deformation plane, π . P_1 and P_2 are the maximum shearing planes.

Observation 2. For a stable cold-rolling texture of $\{hkl\} \langle uvw \rangle$ type, we may observe the equality of shear stress moduli on the most loaded slip systems which are also the most probably active. Because when a slip system comes into effect there is a rotation of the crystal, one can deduce that the equality of shear stresses corresponds to a cancelling of the sum of the rotations due to each system and therefore to the stability of the texture.

Observation 3. The above calculation relating to the equality of the shear stress moduli shows us finally that the most loaded slip systems pointed out in Observation 2 are those which had the normal direction

to the slip plane or the slip direction in the plane, π , in Observation 1.

From these different observations, the following conclusions can be drawn.

1. In a stable texture represented by a crystal in a certain orientation relative to the rolled sheet axis, shear stress moduli are equal on the most loaded glide systems: the common value $\langle H \rangle$ of these stresses is then at a maximum compared with shear stresses on other glide systems in the crystal; $\langle H \rangle$ is also at a maximum relative to the small rotations of the crystal around the equilibrium position.

2. There exists a correlation between the maximum value of a shear stress and a slip element moving into the plane π , the normal direction of a slip plane or slip direction. In fact, it may be demonstrated [30] that a slip element being fixed (the normal direction \mathbf{n} of a slip plane for instance), the shear stress, τ , calculated following Equation 1 is at a maximum when the corresponding slip direction, \mathbf{g} , ($\mathbf{g} \perp \mathbf{n}$) comes into the rolling plane, π . This demonstration uses the Lagrange undetermined coefficient method for calculating extreme values of τ , with the supplementary relationship: scalar product $\mathbf{g} \cdot \mathbf{n} = 0$ ($\mathbf{g} \perp \mathbf{n}$) taken into account. Conversely, if \mathbf{g} is fixed, τ is maximum if \mathbf{n} comes into π .

Hence, these are the two notions of equal and maximum values of shear stress moduli as well as their corollary concerning slip elements moving into plane π , which we intend to develop in a calculation from which the following assumptions may be made.

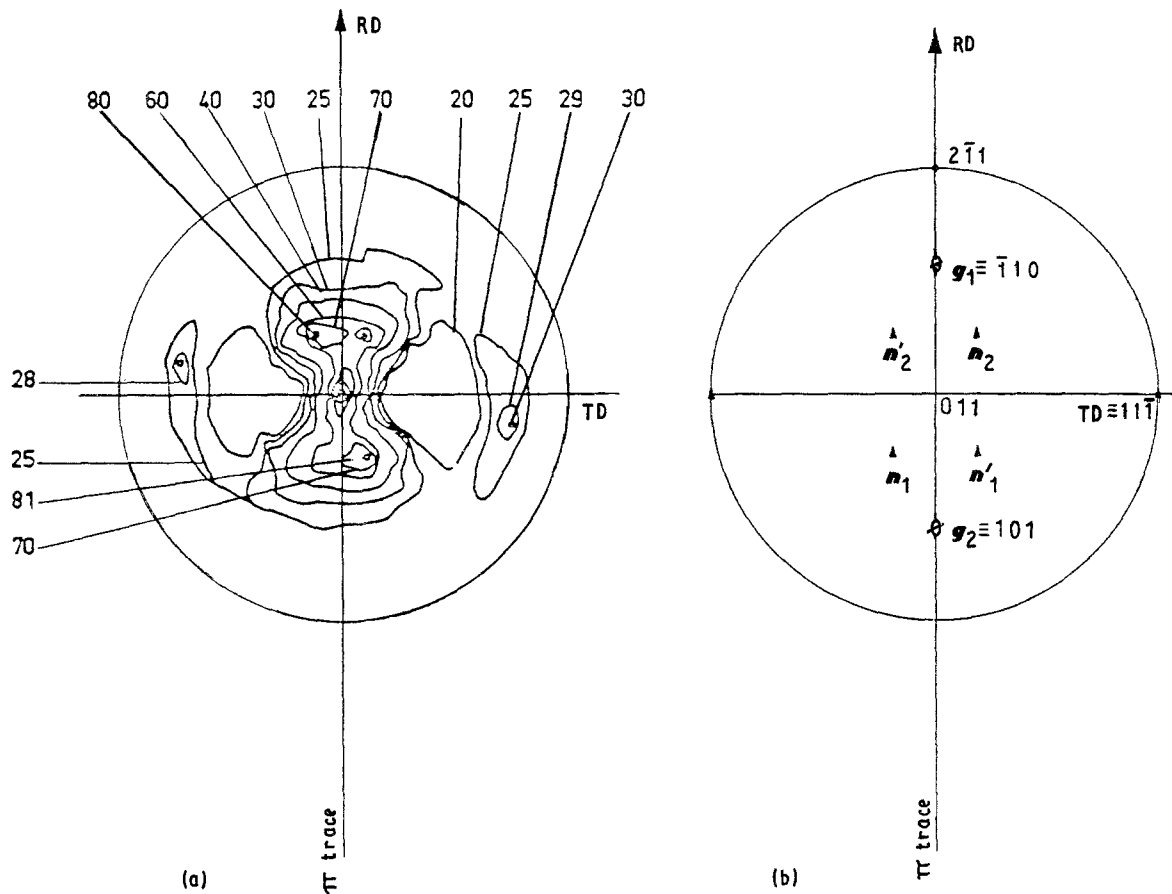


Figure 3 (a) $\{111\}$ pole figure of 90% at 20°C cold-rolled (80-20) α brass. (b) Stereographic diagram corresponding to (a): two slip directions g_1 and g_2 come in π plane. (▲) $\{111\}$, (⊙) $\{110\}$.

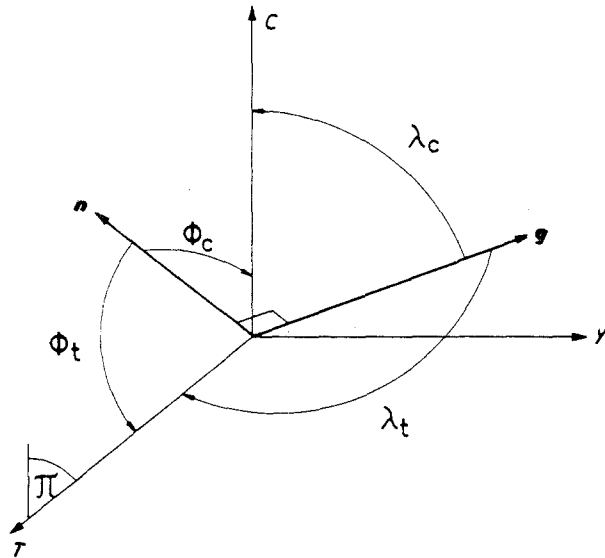


Figure 4 Location of a glide system (n, g) in a trihedral (C, T).

3. Assumptions on deformation by cold rolling

3.1. Plane deformation

Deformation is assumed to be a plane deformation,

$$\varepsilon_3 = 0 \quad (2)$$

deformation in the transverse direction is equal to zero.

This strain, ε_3 , is given by Hooke's laws

$$E\varepsilon_3 = \sigma_3 - \nu(\sigma_1 + \sigma_2) \quad (3)$$

in the elastic field of deformation. At the elastic-plastic transition point, B_0 (Fig. 5) we have both

$$\begin{cases} \varepsilon_3 = 0 & \text{(plane strain)} \end{cases} \quad (4a)$$

$$\begin{cases} \nu = 0.5 & \text{(plastic incompressibility)} \end{cases} \quad (4b)$$

From Equation 3, we can then state at the limit boundary and in the deviatoric tensor [30]

$$\sigma'_3 = 0 \quad (5)$$

if hydrostatic stress is assumed to have no effect on deformation. The same reasoning can be extended to each point B_1, B_2, B_3, \dots , of the loading curve considered as the limits of the elastic segments $A_1B_1, A_2B_2, A_3B_3, \dots$, if it is supposed that residual stresses due to strain hardening cancel each other out, due to the symmetries of deformation by rolling, particularly in the transverse direction along which we have supposed the strain to be $\varepsilon_3 = 0$.

The assumptions

- (i) $\varepsilon_3 = 0$, and
 - (ii) no effect of hydrostatic stress on strain,
- lead in consequence to the deviatoric tensor

$$\begin{cases} \sigma'_3 = 0 \end{cases} \quad (3)$$

$$\begin{cases} \sigma'_1 = -\sigma'_2. \end{cases} \quad (6)$$

If $T = \sigma'_1$, the deviatoric stress in the rolling direction, and $C = \sigma'_2$, the deviatoric stress orthogonal to the

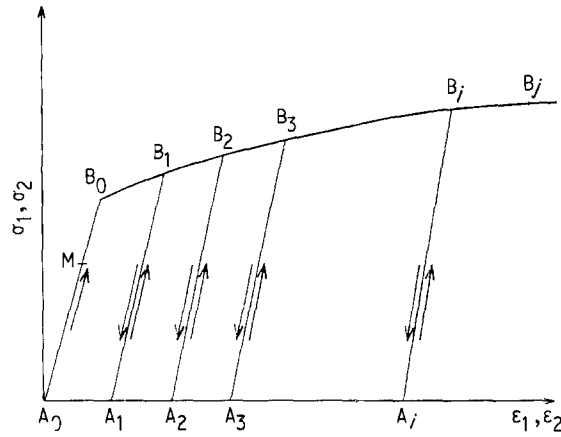


Figure 5 Schematic tensile curve $\sigma_1(\epsilon_1)$ and compression curve $\sigma_2(\epsilon_2)$ corresponding to a cold-rolled material following directions 1 (rolling direction) and 2 (normal direction). This sketch shows evidence of elastic deformation domains A_0B_0 , A_1B_1 , A_2B_2 , ..., A_iB_i , ..., within which the rolled material may stay during loading and unloading cycles (indicated by the arrows on the graph). These cycles can be particularly described at the time of the successive rolling passes.

rolled sheet plane, we have

$$T = -C \quad (7)$$

Hence a Mohr circle centred on the origin of the axis and two maximum shearing planes inclined by $\pi/4$ rad relative to principal directions ND and RD: P_1 and P_2 planes in Fig. 2.

Another demonstration can be made from Hill's theory for anisotropic materials [30]. It consists of showing that the hypothesis $d\epsilon_3 = d\epsilon_{33} = 0$ (zero value of the strain in the transverse direction) leads to $\sigma'_3 = \sigma'_{33} = 0$, if one considers the loading function, f , associated to the second invariant, J_2 , of the stress tensor (Von Mises criteria for an anisotropic material)

$$f = J_2 - k^2 = 0 \quad (8)$$

with

$$J_2 = \frac{1}{H} \sum_{ijkl} C_{ijkl} \sigma_{ij} \sigma_{kl} \quad (9)$$

When using the plastic flow law

$$de_{ij} = \lambda \frac{\partial f}{\partial \sigma_{ij}} \quad (10)$$

we calculate

$$de_{ij} = \frac{2\lambda}{H} \sum_{ijkl} C_{ijkl} \sigma'_{kl} \quad (11)$$

From Equation 11 and taking into account the connections between the coefficients C_{ijkl} [30], it can be shown that the plane strain condition $d\epsilon_{33} = 0$ involves Equation 5, if there is a supplementary condition between coefficients, i.e.

$$C_{1111} = C_{2222} \quad (12)$$

which is legitimate because the rolling direction (1) and the normal direction to the plane of the rolled sheet (2) play similar parts, the first in tension and the second in compression. We therefore obtain as before

$$\begin{cases} \sigma'_3 = 0 \\ \sigma'_1 = -\sigma'_2 \end{cases} \quad (3)$$

$$\sigma'_1 = -\sigma'_2 \quad (6)$$

in the course of plastic strain by cold rolling, hence a state of plane stress in the deviatoric tensor.

3.2. Deformation on slip planes

Crystal deformation is assumed to occur on slip planes, whose normal direction is n_i , and along slip directions g_i , with shear stress

$$\tau_i = (C \cos \lambda_c \cos \phi_c + T \cos \lambda_t \cos \phi_t)_i \quad (13)$$

where τ_i is the deviatoric tensor; this expression comes from hypotheses in Section 3.1, where we have demonstrated that the plane state of strain leads to a biaxial state of stress in the deviatoric tensor, i.e.

$$T = -C \quad (7)$$

Hence, the τ_i expression which will be used in our next calculations is

$$\tau_i = C(\cos \lambda_c \cos \phi_c - \cos \lambda_t \cos \phi_t)_i \quad (14)$$

with $\lambda_c = [g, c]$, $\lambda_t = [g, T]$, $\phi_c = [n, C]$, $\phi_t = [n, T]$ (Fig. 4).

The Boas and Schmid law is therefore considered applicable when both states of tension, T , and compression, C , are superposed.

3.3. Deformation obeying Bishop and Hill's principle

The deformation is assumed to obey Bishop and Hill's maximum plastic work principle. If

$$dW_i = \tau_i d\epsilon_g^i \quad (15)$$

is the plastic work increment produced by the stress, τ_i inducing a plastic strain $d\epsilon_g^i$ on a glide system i , and if

$$dW_i^* = \tau_i^* d\epsilon_g^i \quad (16)$$

is the work produced by another stress, τ_i^* , being on or inside the yield surface of the material and susceptible to lead to the same strain increment $d\epsilon_g^i$, the maximum plastic work principle, which follows from the second principle of thermodynamics, allows us to state

$$dE = dW_i - dW_i^* = (\tau_i - \tau_i^*) d\epsilon_g^i \geq 0 \quad (17)$$

see Appendix 1. It follows that

$$|\tau_i| \geq |\tau_i^*| \quad (18)$$

between several shear stresses which may cause the same plastic strain increment $d\epsilon_g^i$; the shear stress to be retained is the maximum stress. So, it can be seen that the condition of a maximum shear stress that we have previously observed by experiment and calculation is related to an energetic concept which governs an irreversible transformation.

Another consideration can be added. Suppose

$$dW = C d\epsilon_c + T d\epsilon_t \quad (19)$$

the macroscopic plastic work increment with $d\epsilon_c$ and

$d\varepsilon_T$ strain increments along C and T , and

$$d\varepsilon_c = -d\varepsilon_T \quad (d\varepsilon_3 = 0) \quad (20)$$

and

$$C = -T \quad (7)$$

we have

$$dW = 2Cd\varepsilon_c \quad (21)$$

Moreover, we can state

$$dW = \sum_i \tau_i d\varepsilon_g^i \quad (16)$$

which is the sum of all the plastic work increments on slip systems i .

By decomposition in exact total differential

$$2Cd\varepsilon_c = \sum_i \tau_i d\varepsilon_g^i \quad (22)$$

It follows that

$$\left| \frac{\partial \varepsilon_c}{\partial \varepsilon_g^i} \right|_{c, \tau_i} = \frac{|\tau_i|}{2C} \quad (23)$$

$|\tau_i|$ having a maximum value at crystal equilibrium, $|\partial \varepsilon_c / \partial \varepsilon_g^i|$ will be the same: during deformation, each crystal will simultaneously look for a maximum macroscopic deformation and a minimum deformation on an atomic scale.

The energetic considerations of this section are essential to explain the rotations and the final equilibrium positions of each crystal during cold rolling.

3.4. Rotation of the crystal

In analogy with uniaxial tensile and compressive tests and by slipping on one or several glide systems, one crystal tends to bring the normal direction to the slip plane near the compression axis C and the slip direction near the tensile axis T .

3.5. Crystal stability

Rolled crystal stability is obtained when the sum of the different rotations due to the different glide systems is reduced to zero. Each glide system contribution to rotation, which is represented by the expression $\partial \varepsilon_c / \partial \varepsilon_g^i$ is then the same in modulus. From Equation 23 it can be seen that we obtain the equality of the shear stresses $|\tau_i|$ which are therefore equal to a common and maximum value \bar{H} .

3.6. Extensions to polycrystal

Deformation by rolling being assumed to be a plane deformation, the compatibility of the strains is assumed to be effective between crystals at grain boundaries, when Boas' and Schmid's model is applied.

4. Stability criteria of a cold-rolling texture

As a result of the above hypothesis, our theory allows us to set forth three stability criteria of a rolling

texture represented by a crystal oriented $\{hkl\} \langle uvw \rangle$ which is deformed by the action of p glide systems.

Criterion 1. At equilibrium, there is equality of shear stress moduli in the deviatoric tensor on the p glide systems considered

$$|\tau_1| = |\tau_2| = |\tau_3| = \dots = |\tau_p| = \bar{H} \quad (24)$$

Criterion 2. Value \bar{H} is maximum (relative to other shear stresses in the crystal and relative to other values taken by \bar{H} for a slight disorientation of the crystal around its equilibrium position).

This condition is satisfied, to the extent of the possibilities given by crystal symmetries, when a normal direction to an active slip plane or an active slip direction at least belongs to the deformation plane π .

Criterion 3. At this point and from the fact that the $|\tau|$ expression is invariable in a permutation of C and T , there is lack of determination for choosing between the two textures $\{hkl\} \langle uvw \rangle$ and $\{uvw\} \langle hkl \rangle$. To determine the stable texture, it is necessary to call for the "followed path" as understood by the second principle of thermodynamics and in accordance with the hypothesis given in Section 3.4: the texture so defined is such that the active plane normal direction, which is the nearest to plane π (or which belongs to π), is also the nearest to compressive direction C , and similarly, for the active slip direction relative to the tensile direction T .

Each stable texture will be characterized by its stability factor $m = \bar{H}/C$. The greater \bar{H} and then m are, the more stable will be a given texture [30, 31].

5. Application to the stability of a cold-rolled crystal

5.1. Simple slip

Fig. 6 shows different configurations encountered when applying the three criteria. To have a maximum shear stress, we must have either one or two slip elements in plane π . The transverse direction is then crystallographically determined. One can then write the equality of the moduli of the shear stresses for all the glide systems for which one element belongs to π . Criterion 3 allows the stable texture to be chosen from the two still possible.

5.2. Slip with mechanical twinning

If there is mechanical twinning in addition to slipping, two half-crystals in twinning position will reach their equilibrium position when the three criteria are satisfied, respectively, for each half-crystal: a sufficient condition will be that two common crystallographic and slipping elements for the two half-crystals come in plane π , if they exist. As the whole of the common elements of the two half-crystals are contained in the twinning plane, we can conclude that a sufficient condition of equilibrium for the twins is that the twinning plane becomes parallel to π (Fig. 7). The transverse direction is then determined and we return to the demonstration in Section 5.1.

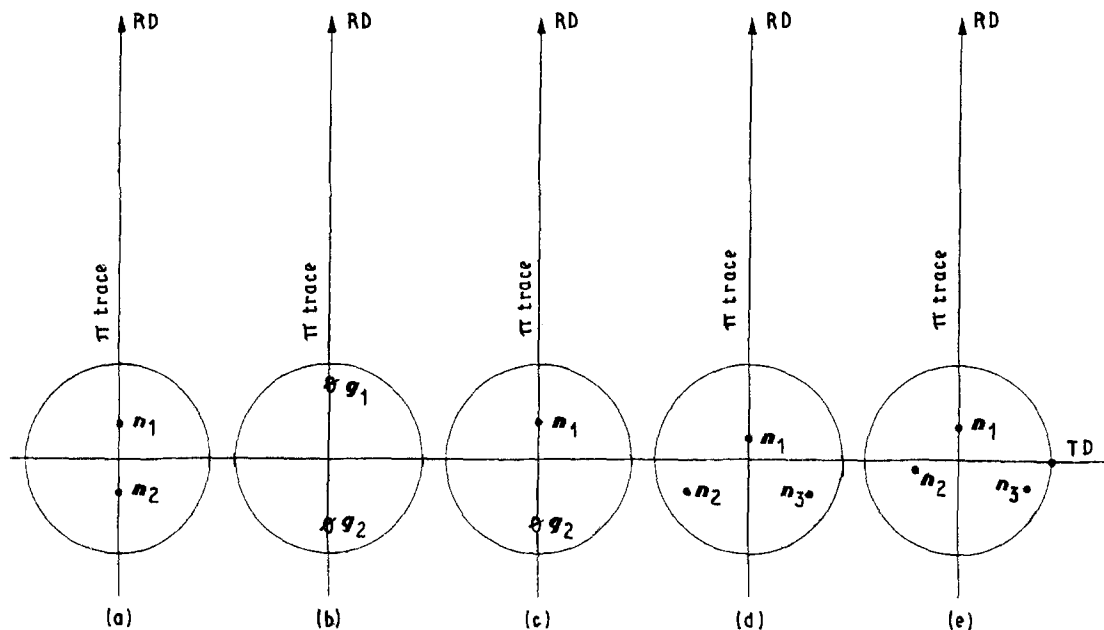


Figure 6 Summary of different slip element combinations which ensure crystal stability. n , normal direction to a glide plane. g , slip direction.

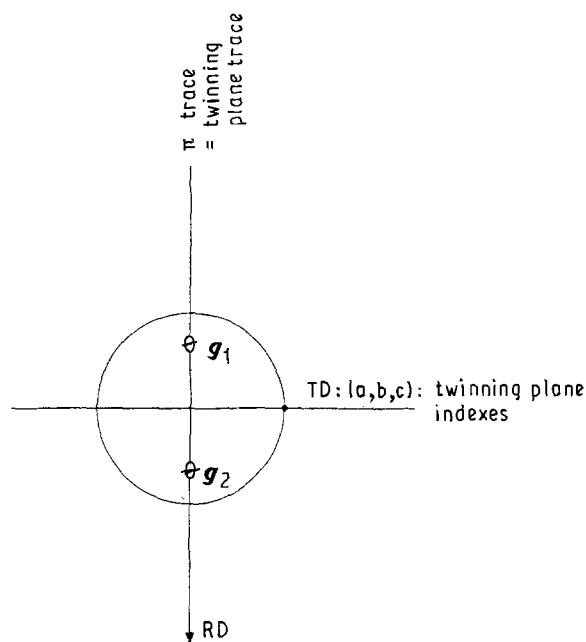


Figure 7 Stable orientation of two grains in twinning position. Slip directions g_1 and g_2 , common to both grains, are in the π plane (Criterion 2), which means the twinning plane is in coincidence with π .

5.3. Application to polycrystals

The above three criteria enable prediction of stability conditions for a crystal straining by slipping and twinning. In the polycrystalline aggregate and in accordance with the assumption in Section 3.6, one crystal will take on either one orientation or another depending on its initial position in the non-deformed aggregate. If the initial orientation distribution of the crystallites is random, the apparition frequency of a stable texture will be more, the greater is $m = \frac{H}{C}$, in application of Criterion 2. If the initial distribution of crystallites is not random, the observed final textures for a major deformation of the aggregate will be qualitatively but not quantitatively the same as before. It will then be necessary to examine the evolution of

each initial texture during cold rolling, in accordance with the assumption in Section 3.4.

6. Application to body-centred cubic metals

Let us return to the low index textures which the authors consider to be stable: $\{112\} \langle 110 \rangle$, $\{001\} \langle 110 \rangle$, $\{111\} \langle 112 \rangle$. The glide systems which we shall use for the application of the three criteria are $\{110\} \langle 111 \rangle$ and $\{112\} \langle 111 \rangle$.

As indicated previously and following Fig. 6, the review of the different crystalline configurations having the property to put one or two slip elements in π , together with a simple calculation, allow up to 20 stable textures to be determined; these are indexed in Table I. One can recognize in this table the three textures with low indices previously discussed. The theory enables experimental results to be retrieved.

It is interesting to note from this table that texture (a): $\{001\} \langle 110 \rangle$, which seems to be the most stable by virtue of its m value (0.943), owes its equilibrium to antagonistic (in rotation for the crystal) glides on planes $\{112\}$. This can indeed be verified on the sections orthogonal to the rolling direction and to the transverse direction of the parallelepipedic and mono-crystalline Fe-3% Si and cold-rolled 50% in the orientation $\{001\} \langle 110 \rangle$ sample: on the section cut orthogonal to the rolling direction, slip lines are parallel (Fig. 8a); on the section cut orthogonal to the transverse direction they are crossed (Fig. 8b), which reveals that slip planes have their normal direction in plane π defined by RD and ND. We should specify that the technical method of rendering these slip lines visible consists of camping out slight additional cold rolling after polishing the surfaces to be examined on the sample already rolled to 50% thickness.

Finally, it may be noted that slip plane traces on the transverse section correspond angularly to plane $\{112\}$ traces, which confirms the calculation (Fig. 8b).

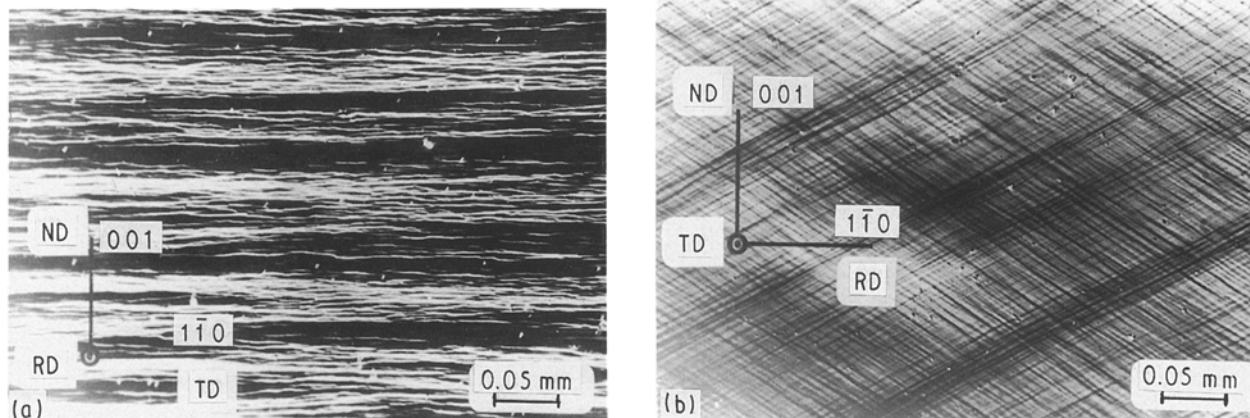


Figure 8 (a) 50% cold-rolled monocrystalline Fe-Si (3%) in the orientation $\{001\} \langle 1\bar{1}0 \rangle$, viewed along the rolling direction, RD. Mechanical revealing of glide traces. (b) Same sample as (a) but viewed along the transverse direction, TD.

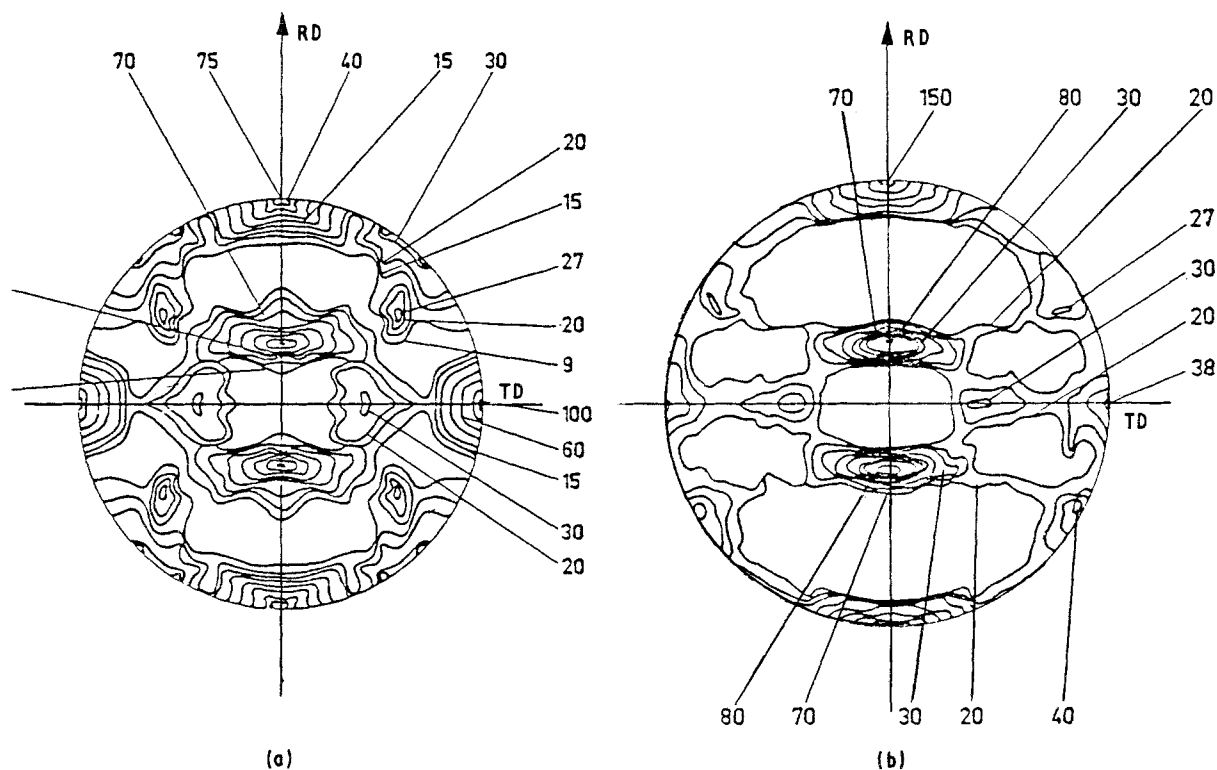


Figure 9 (a) $\{110\}$ theoretic pole figure of a highly cold-rolled body-centred cubic metal. (b) $\{110\}$ pole figure of 90% cold-rolled high-purity iron.

With regard to twinning, we have considered texture i in Table I for which a twinning plane $\{112\}$ is parallel to π . We obtain a calculated texture $\{3104\} \langle 14523 \rangle$ which is not significant because of its asymmetry relative to the rolling axis and also because of the existence of other possible textures due to the numerous possibilities of slipping in cubic-centred metals. It can be added, moreover, that body-centred cubic metals have less tendency to twin than face-centred cubic metals.

From this, we may deduce the absence of a characteristic twinning texture in body-centred cubic metals, which is confirmed by experiment.

These results, particularly those shown in Table I, may be plotted on a stereographic projection, each texture being represented by a single type of plane as in a pole figure obtained from X-ray examination. Each point so defined is given the m value of the corresponding texture, this value being assumed to evaluate

the probability of the considered texture appearing. The calculated pole figure is then obtained by drawing the equi- m lines (Fig. 9a). It can be seen that this figure is very similar to the experimental pole figure (Fig. 9b), which confirms the validity of our three criteria.

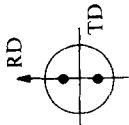
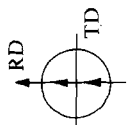
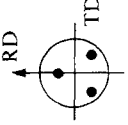
7. Application to face-centred cubic metals

The originality of face-centred cubic metals relative to body-centred cubic metals, is that they present three types of texture which can be related to the stacking fault energies of these metals.

(i) the copper-type texture, characterized by a preponderant texture close to $\{112\} \langle 111 \rangle$, corresponds to stacking fault energies of order of about 60 erg cm^{-2} [32].

(ii) the α -brass-type texture, the characteristic orientation of which is $\{110\} \langle 112 \rangle$, this texture also

TABLE I. Summary of body centred cubic metal rolling textures

Slipping mode ^a	TD	Texture	Notation	m^b
2 slip planes 	$\{110\}$	$\langle 111 \rangle$ $\langle 100 \rangle$	$\{112\} \langle 110 \rangle$ $\{001\} \langle 100 \rangle$	0.816 0.816
	$\{112\}$	$\langle 110 \rangle$ $\langle 311 \rangle$ $\langle 012 \rangle$	$\{001\} \langle 110 \rangle$ $\{321004\} \langle 10420332 \rangle$ $\{120\} \langle 001 \rangle$	(a) 0.943 0.687 0.472
	$\{110\} + \{112\}$	$\langle 311 \rangle$ $\langle 110 \rangle$	$\{81135\} \langle 4611325 \rangle$ $\{807373\} \langle 734040 \rangle$	0.852 0.560
2 slip directions $\langle 111 \rangle$ 	On 2 planes $\{112\}$ On 3 planes $\{112\}$ On 2 planes $\{110\}$ and 1 plane $\{112\}$	$\langle 110 \rangle$ $\langle 110 \rangle$ $\langle 110 \rangle$	Texture (a): $\{001\} \langle 110 \rangle$ $\{356100100\} \langle 200356356 \rangle$ $\{1411\} \langle 21414 \rangle$	0.943 (b) (c) 0.457 0.857
3 slip planes, a normal to one of them being in π 	$\{110\}$	$\langle 110 \rangle$ $\langle 100 \rangle$	$\{111\} \langle 112 \rangle$ $\{072100\} \langle 010072 \rangle$	(d) 0.545 0.259
	$\{112\}$	$\langle 110 \rangle$ $\langle 110 \rangle$ $\langle 110 \rangle$ $\langle 110 \rangle$	$\{123100100\} \langle 200123123 \rangle$ $\{273100100\} \langle 200273273 \rangle$ $\{112100100\} \langle 200112112 \rangle$ Texture (b): $\{356100100\} \langle 200356356 \rangle$	(f) (g) 0.468 0.272 0.541 0.457
	1 plane $\{110\}$ (the normal of which $\in \pi$: and 2 planes $\{112\}$)	$\langle 110 \rangle$ $\langle 110 \rangle$ $\langle 110 \rangle$ $\langle 100 \rangle$ $\langle 100 \rangle$ $\langle 100 \rangle$	$\{96060\} \langle 12099 \rangle$ $\{64210001000\} \langle 2000642642 \rangle$ $\{28100100\} \langle 2002828 \rangle$ $\{08571000\} \langle 01000857 \rangle$ $\{022100\} \langle 010022 \rangle$ $\{05771000\} \langle 01000577 \rangle$	(h) 0.239 0.435 0.220 0.125 0.740 0.408
	1 plane $\{112\}$ (the normal of which $\in \pi$) and 2 planes $\{110\}$	$\langle 110 \rangle$	Texture (c): $\{1411\} \langle 21414 \rangle$	0.857

3 slip directions $\langle 111 \rangle$, one of which $\in \pi$	Results included in the preceding lines	$\langle 110 \rangle$ $\langle 110 \rangle$	Textures (d), (e), (f), (g), (h) and $\{12^{1/2}1\} \langle 12^{1/2}1 \rangle^*$ *On $\{110\}$ slip planes	0.289
1 plane + 1 slip direction	Textures already obtained: $\{112\}$ in $\pi + \langle 111 \rangle$ in π $\{110\}$ in $\pi + \langle 111 \rangle$ in π	$\langle 110 \rangle$ $\langle 123 \rangle$ $\langle 112 \rangle$	Textures (b), (c), (d), (h) $\{633\}386\ 550\} \langle 122\ 214\ 10 \rangle$ $\{3\ 10\ 4\} \langle 14\ 5\ 23 \rangle$	0.370 0.805

^a TD, transverse direction; RD rolling direction.
^b $m = \frac{a}{c}$ is the characteristic factor of the texture.

being observed in cold-rolled silver, corresponds to stacking fault energies close to 20 erg cm^{-2} . This texture is also obtained by rolling, at very low temperatures, face-centred cubic metals which have a copper-type texture at room temperature.

(iii) The cerium-type texture defined by planes $\{111\}$ on the surface of the rolled sheet is correlated with very low stacking fault energies.

The following textures should also be added: $\{110\} \langle 001 \rangle$ and $\{001\} \langle 100 \rangle$, which can be observed by experiment [16].

7.1. Hypothesis of the single slip $\{111\} \langle 110 \rangle$ type

For face-centred cubic crystals, the glide systems being $\{111\} \langle 110 \rangle$ type, calculations made as formerly for body-centred cubic metals are given in Table II. Examination of this table again reveals the textures obtained by experiment of face-centred cubic metals; but this is only qualitative because the calculated pole figure gives a result which is not similar to either copper- or α -brass- or cerium-type textures for high deformations (Fig. 10). One can therefore think that other phenomena than single $\{111\} \langle 110 \rangle$ glide come into play for major strain hardening.

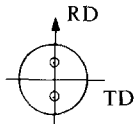
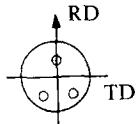
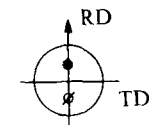
7.2. $\sim \{112\} \langle 111 \rangle$ copper-type texture: due to $\{111\} \langle 110 \rangle$ glide + $\{001\} \langle 100 \rangle$ glide for high deformations

Observations in high-purity (OFHC) copper monocrystals cold rolled in the orientation $\{112\} \langle 111 \rangle$ have shown, for rolling deformations greater than 50% thickness, the appearance of strain strips within which slip lines corresponding to slip planes $\{001\}$ have been distinguished [33] Fig. 11a-c. Polishing-corrosion tests moreover revealed alignments of emergence points of crystalline defects that we have explained as dislocations, whose Burgers' vector was not $\mathbf{b} = \frac{a}{2} [110]$ standard type, these last dislocations having no reaction during polishing under the given conditions (Fig. 12). $\{001\} \langle 100 \rangle$ slip lines having finally been observed during shearing tests on OFHC copper monocrystals preliminarily strain hardened by cold rolling and sheared in the plane (001) in the direction $[100]$ (Fig. 13). We have assumed that the slip lines observed in the strain strips of the previous $\{112\} \langle 111 \rangle$ rolled monocrystal were characteristic of glide $\{001\} \langle 100 \rangle$.

With regard to this type of glide, it may be stated that glide on planes $\{001\}$ has already been noted by several authors [26-29] and that the Burgers' vector dislocation, $\mathbf{b} = a [010]$, established for plain cubic crystallographic model, has been observed by electron microscopy in slightly disoriented flexion grain boundaries: 1° around $[001]$ in aluminium bicrystals [34].

The energy of this dislocation is not much greater than the energy of the standard $\langle 110 \rangle$ dislocation elsewhere (see Appendix 2); it is then possible that $\langle 100 \rangle$ dislocation exists from the thermodynamic point of view.

TABLE II Summary of face centred cubic metal rolling textures. $\{111\} \langle 110 \rangle$ glide type only

Slipping mode		TD	Texture	Notation	m
2 slip planes	$\{111\}$	$\langle 110 \rangle$	$\{110\} \langle 001 \rangle$	(a)	0.816
2 slip directions	$\langle 110 \rangle$	$\langle 111 \rangle$	$\{110\} \langle 112 \rangle$		0.816
		$\langle 100 \rangle$	$\{001\} \langle 100 \rangle$		0.816
					
3 slip planes, a normal to one of them being in π	$\{111\}$	$\langle 110 \rangle$	$\{112\} \langle 111 \rangle$	(b)	0.545
		$\langle 110 \rangle$	$\{12^{1/2}1\} \langle 12^{1/2}1 \rangle$		0.289
3 slip directions, one of them $\in \pi$	$\langle 110 \rangle$	$\langle 110 \rangle$	Texture (b): $\{112\} \langle 111 \rangle$		0.545
		$\langle 100 \rangle$	$\{072100\} \langle 010072 \rangle$		0.259
					
1 plane + 1 slip direction	$\{111\} + \langle 110 \rangle$	$\langle 110 \rangle$	Texture (b): $\{112\} \langle 111 \rangle$		0.545
					

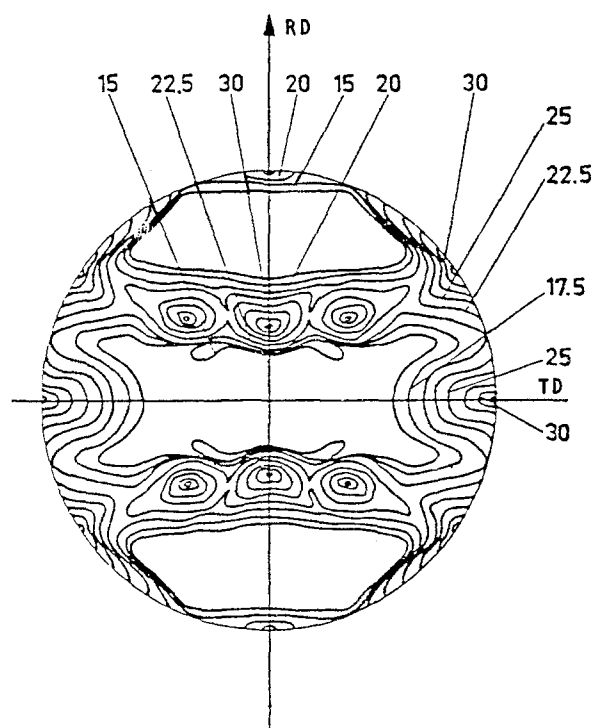
Figure 10 $\{111\}$ theoretical pole figure of a highly cold-rolled face-centred cubic metal ($\{111\} \langle 110 \rangle$ single glide assumption: compiling of Table II textures).

Fig. 14 allows us to locate a $[100]$ direction in the $(211) [\bar{1}11]$ texture. We can see that this direction belongs to plane π : it is therefore particularly well oriented to be an active normal direction to a slip plane or an active slip direction (Criterion 2).

Table III enables definition of some additional textures which result from the action of this "cubic" glide

system. We can then, as above, draw a pole figure calculated by taking account of both Tables II and III for copper-type texture. It can be seen that we obtain a pole figure very close to the experimental pole figure for copper (Fig. 15a and b), which justifies our different assumptions on cold rolling (the three criteria) and on the occurrence of $\{001\} \langle 100 \rangle$ glide in highly cold-rolled pure copper.

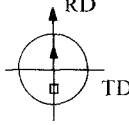
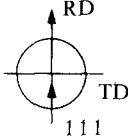
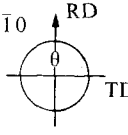
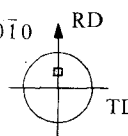
7.3. $\{110\} \langle 112 \rangle$ α -brass-type texture: due to mechanical twinning $\{111\} \langle 112 \rangle + \{111\} \langle 110 \rangle$ glide

This second type of texture is found when mechanical twinning occurs during the course of deformation as a result of either rolling of a face-centred cubic metal at a very low temperature or rolling of a face-centred cubic metal, the stacking fault energy of which is lower than in the preceding copper-type textures (Section 7.2): α -brass and silver have, in fact, energies close to 20 erg cm^{-2} .

As has been previously stated in Section 5.2, the equilibrium position of the twinned crystal will be reached when the twinning plane $\{111\}$ is parallel to the plane π ; the transverse direction will then be defined as $\langle 111 \rangle$, and the application of Criterion 1 to the equality of shear stresses allows us to calculate the equilibrium texture $\{110\} \langle 112 \rangle$. It should be noted that the general textures given in Table II are always valid for α -brass: they concern grains having sustained no twinning during rolling.

$\{110\} \langle 112 \rangle$ texture already appears in Table II and, in fact, experiment shows that this texture is stable in monocrystalline copper cold rolled to very

TABLE III Summary of face centred cubic metal rolling textures. Copper-type texture: textures from Table II and additional textures due to $\{001\} \langle 100 \rangle$ glide (following)

Slipping mode		TD	Texture	m
2 slip planes	$\{111\} + \{100\}$ S1: $\{111\} \langle 110 \rangle$ S2: $\{100\} \langle 001 \rangle$	$\langle 110 \rangle$	$\{23\ 10\ 10\} \quad \langle 20\ 23\ 23 \rangle$	0.629
				
4 slip systems	1st case	$\langle 110 \rangle$	$\{20\ 50\ 26\} \quad \langle \overline{115}\ 86\ \overline{77} \rangle$	0.656
S1: $\{111\} \langle 1\overline{1}0 \rangle$ S2: $\{\overline{1}11\} \langle 101 \rangle$ S3: $\{100\} \langle 0\overline{1}0 \rangle$ S4: $\{010\} \langle 100 \rangle$				
	2nd case	$\langle 110 \rangle$ $\langle 110 \rangle$	$\{1\overline{1}0\}$ $\{1\overline{1}0\}$ 1st solution: $\{20\ 50\ 28\} \quad \langle \overline{33}\ 29\ \overline{28} \rangle$ 2nd solution: $\{7\ 1\ 10\} \quad \langle \overline{31}\ 17\ 20 \rangle$	0.622 0.367
				
	3rd case	$\langle 110 \rangle$ $\langle 110 \rangle$	$\{0\overline{1}0\}$ $\{0\overline{1}0\}$ 1st solution: $\{4\ 15\ \overline{12}\} \quad \langle 15\ \overline{40}\ \overline{45} \rangle$ 2nd solution: $\{15\ \overline{40}\ \overline{45}\} \quad \langle 4\ 15\ \overline{12} \rangle$	0.320 0.320
				

Notes: 1. α brass-type texture: textures from Table II + twinning: $\{110\} \langle 112 \rangle$ texture favoured.
2. Cerium-type texture: compact hexagonal metal texture: $\{0001\} \langle 1120 \rangle$ which is equivalent to face-centred cubic $\{111\} \langle 110 \rangle$.
3. Meaning of used symbols in Tables I, II and III: (\odot) slip element (normal to a plane or slip direction), (\bullet) normal to a slip plane: (\blacktriangle) = $\{111\}$; (\square) = $\{100\}$, (θ) slip direction: $\langle 110 \rangle$.

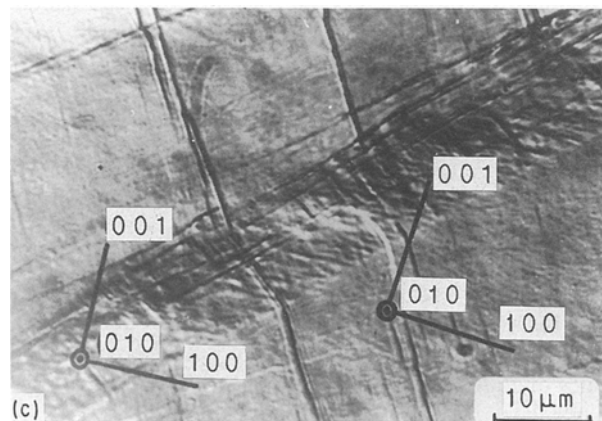
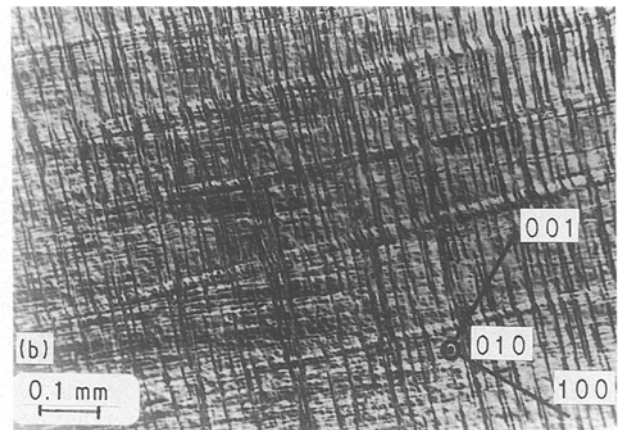
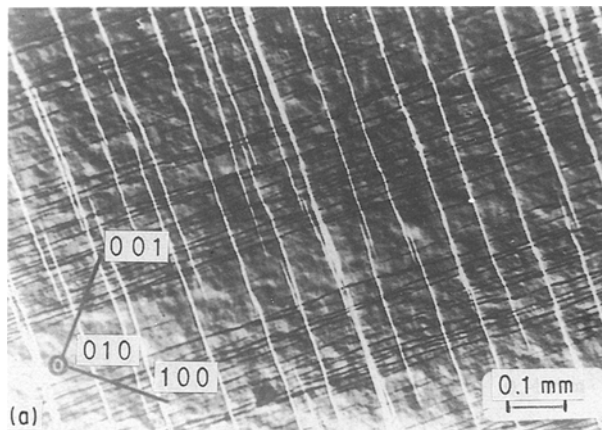


Figure 11 (a) 45% cold-rolled monocrystalline OFHC copper (010) face observation: $\{111\}$ slip plane traces only are visible. The sample is rolled in the stable $\{112\} \langle 111 \rangle$ orientation. (b) Observation of the same face for 55% cold rolling: strain strips appear over the whole sample. (c) Detail of the inside of a strain strip: traces of (001) slip planes are visible and only one family – that most loaded by shearing.

high deformations [16], but it is more abundant in the presence of twinning, at the expense of other texture components.

Given the existence of twelve twinning systems $\{111\} \langle 112 \rangle$, we have admitted that this $\{110\} \langle 112 \rangle$ texture has a probability 12 times greater of appearing in the presence of twinning: we have thus

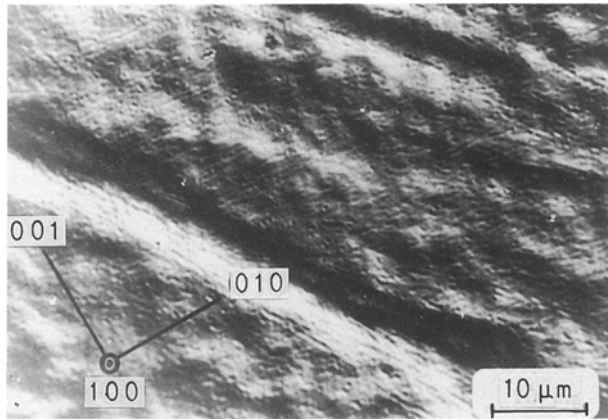


Figure 12 [100] traces drawn by emergence points of defects being in (001) planes of the matrix, these defects not being constituted by standard dislocations with $\langle 110 \rangle$ Burgers vector. We have proposed the assumption in order that these defects may be $\langle 100 \rangle$ Burgers vector dislocations. Orthophosphoric acid polishing, corrosion of 55% cold-rolled OFHC copper [30, 33].

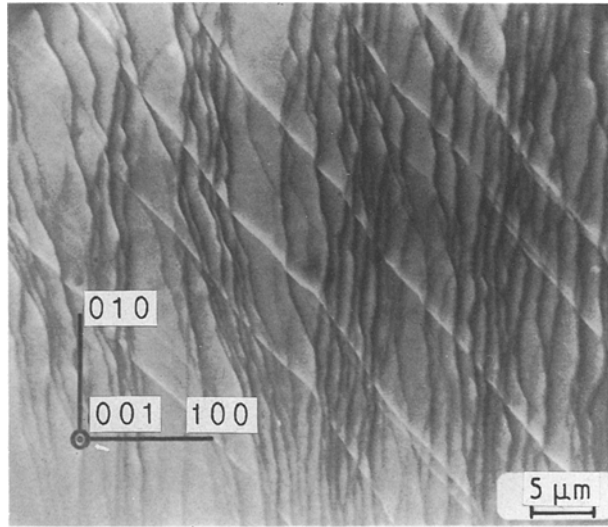


Figure 13 (001) face view on a shear test piece. Shearing on (100) [010] allows glide on (100) planes to be observed, showing up a new type of $\{100\} \langle 010 \rangle$ "cubic" glide [30, 33].

obtained a calculated pole figure which has the general characteristics of an experimental pole figure (Fig. 16a and b) but with quantitative differences. These differences may be explained by the fact that the tendency for a face-centred cubic metal to twin is dependent both on its chemical composition and on the test temperature, which would merit further investigation.

7.4. $\{111\}$ in sheet surface: cerium-type texture: face-centred cubic \rightarrow compact hexagonal allotropic change and glide on $\{10\bar{1}1\}$ pyramidal type slip planes

The stacking fault energy of cerium being particularly low, cold rolling will cause intensive stacking faults to appear on $\{111\}$ planes, this phenomenon being sufficient to cause, partially at least, a face-centred cubic lattice to change to a compact hexagonal crystallographic lattice [16, 35]. One must then consider cold

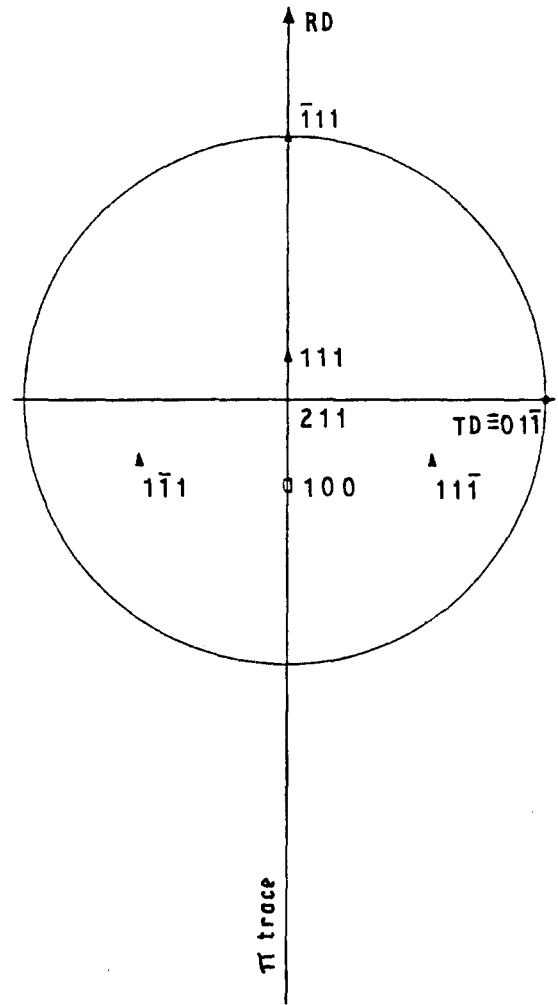


Figure 14 $\{112\} \langle 111 \rangle$ copper texture. Stereographic position of a $\{100\}$ plane.

rolling of a compact hexagonal crystal which will deform by slipping with equal quantities on $\{10\bar{1}1\}$ pyramidal type planes along $\langle 11\bar{2}0 \rangle$ slip directions and in accordance with the three stability criteria.

Nevertheless, if we put two normal directions $\langle 10\bar{1}1 \rangle$ to slip planes in the plane π , following the second criteria, we observe that corresponding slip directions $\langle 11\bar{2}0 \rangle$ are along the transverse direction DT. Then, $\langle H \rangle = 0$ (exceptional case of Criterion 2) (Fig. 17a). In this configuration and given the reduced possibilities of slipping in the compact hexagonal system, we can only comply with the three criteria by considering another crystal orientation for which there are no slip elements in π . One obtains by this means, the $\{0001\} \langle 11\bar{2}0 \rangle$ texture equivalent to the $\{111\} \langle 110 \rangle$ face-centred cubic texture corresponding to the face-centred cubic epitaxial remaining part of the rolled metal (Fig. 17b). The theory then enables us to retrieve the experimental texture with $\{111\}$ planes on the sheet surface.

It may be observed that glide on base plane $\{0001\}$ will not be able, given the unique nature of this plane and the low symmetries of the compact hexagonal system, to be counterbalanced in rotation by other types of glide, except to lead to metastable or unstable textures that we have not calculated.

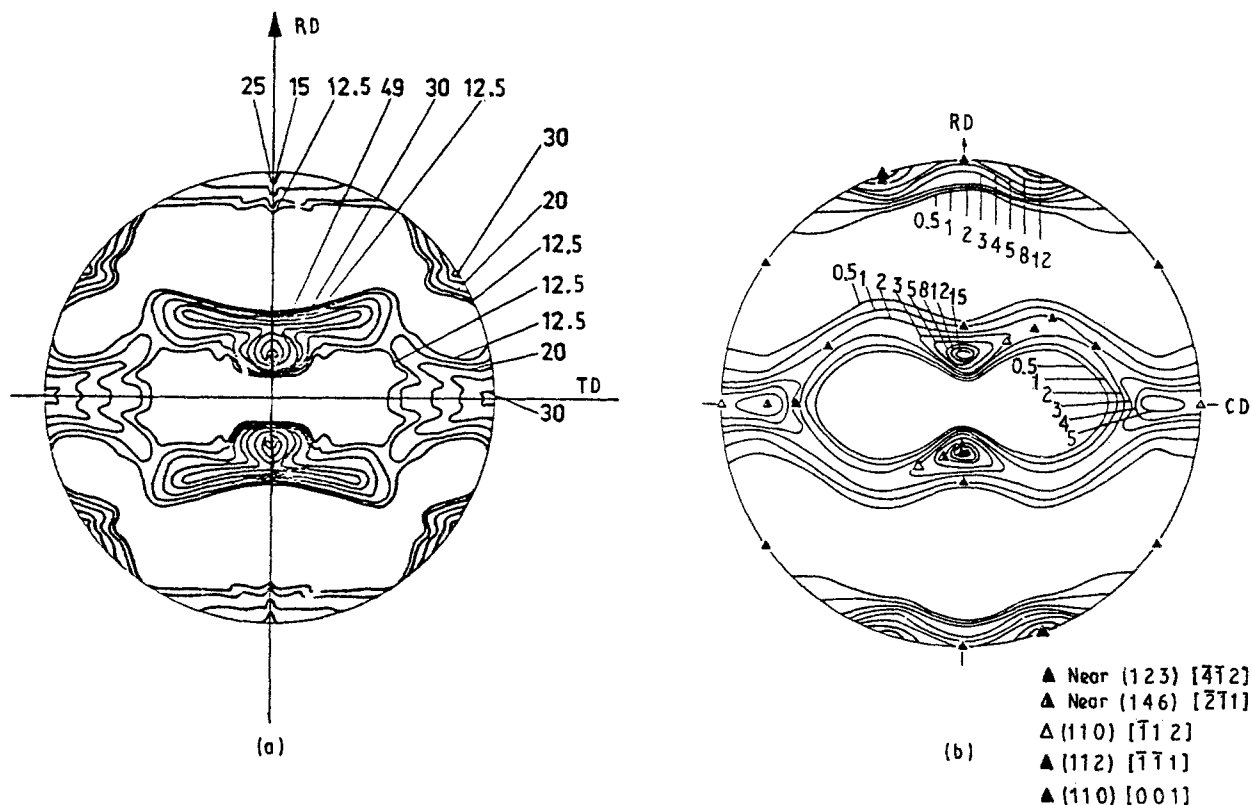


Figure 15 (a) $\{111\}$ theoretical pole figure of highly cold-rolled OFHC copper (obtained from Tables II and III). (b) $\{111\}$ pole figure of 96.6% at 25°C cold-rolled copper (from [16]).

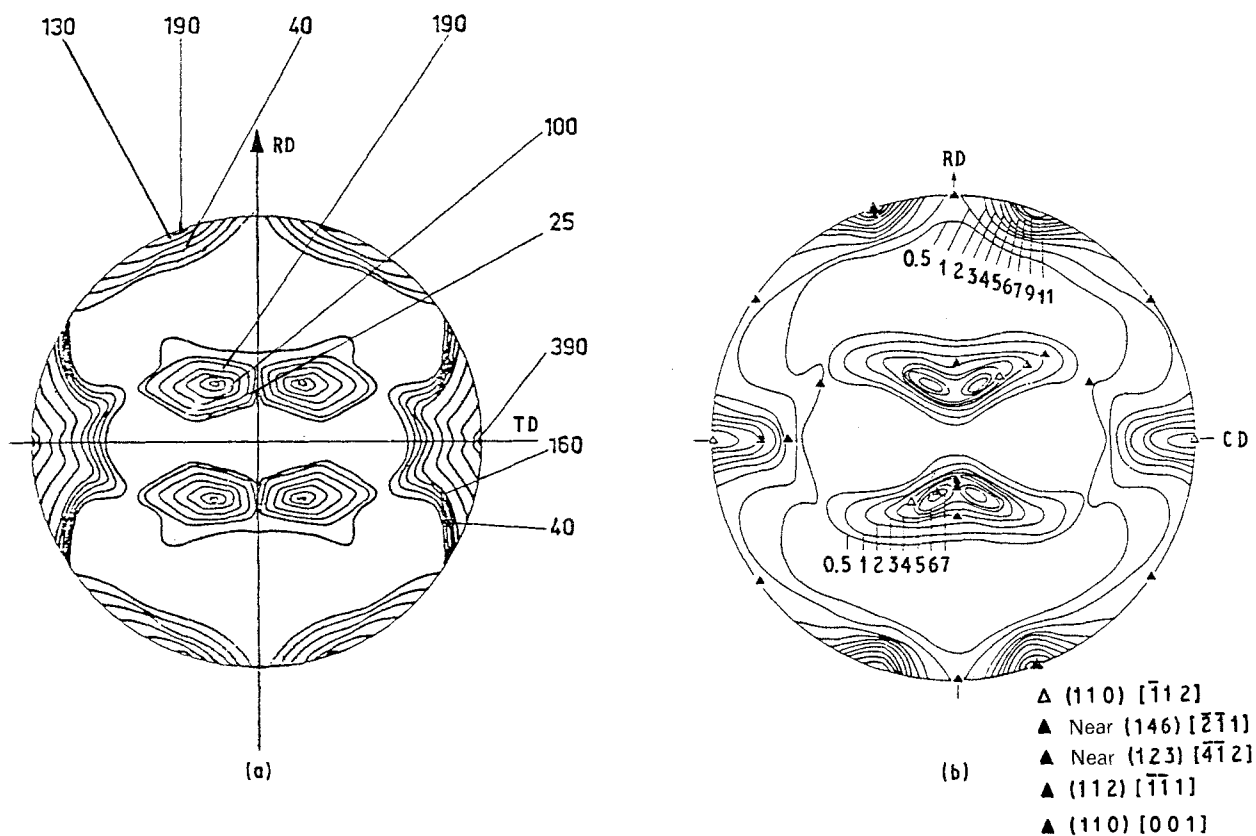


Figure 16 (a) $\{111\}$ theoretical pole figure of highly cold-rolled α -brass. (b) $\{111\}$ pole figure of 96.6% at -196°C cold-rolled electrolytic copper. This texture is α -brass-type (from [16]).

8. Conclusion

This study has enabled us, on the basis of observations made on experimental body-centred cubic and face-centred cubic metal pole figures, to establish three

stability criteria for a cold rolling texture [31]. This three-criteria application has allowed us to retrieve, by calculation, the standard textures observed in cubic metals and some additional less well-known textures,

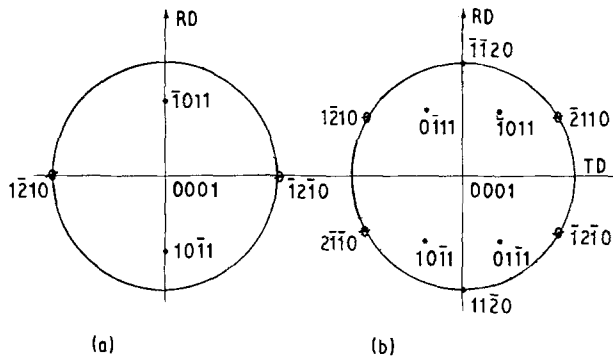


Figure 17 Cerium-type textures. (a) $\tau = 0$, (b) texture $\{0001\} \langle 11\bar{2}0 \rangle$.

the compilation of which, on calculated pole figures, has revealed plotted drawings very similar to experimental stereographic drawings.

Considered assumptions, which characterized cubic metal deformation, concerned glide and twinning systems.

1. $\{110\} \langle 111 \rangle$ and $\{112\} \langle 111 \rangle$ glides for body centred cubic metals. $\{112\} \langle 111 \rangle$ twinning has revealed not to give any specific calculated texture, which is confirmed by experiment.

2. $\{111\} \langle 110 \rangle$ glide for face centred cubic metals, to which we had to add the following assumptions.

(a) $\{001\} \langle 100 \rangle$ "cubic" slip for copper-type texture;

(b) $\{111\} \langle 112 \rangle$ twinning for α -brass-type texture and likewise silver and face-centred cubic metals rolled at very low temperature;

(c) allotropic transformation: face-centred cubic \rightarrow compact hexagonal in the case of a cerium-type texture ($\{111\}$ planes on surface of the sheet).

The fact that the results of experiments agree well with the calculations, proves the validity of our different assumptions [30].

Appendix 1. Maximum plastic work principle

Suppose a stress, σ (σ_{ij} components), which induces a plastic strain $d\epsilon^P$ ($d\epsilon_{ij}^P$ components). The end of σ vector is on the yield surface $f = 0$ and $d\epsilon^P$ vector is orthogonal to this surface: in fact, $d\epsilon_{ij}^P = d\lambda(\partial f / \partial \sigma_{ij})$ (normality condition).

Suppose another stress, σ^* (σ_{ij}^* components), the representative vector's end of which is on or within the yield surface. Suppose that σ^* induces the same strain $d\epsilon^P$ as σ . In this deformation, σ sustains a stress increment, $d\sigma$, the vector of which is tangential to the yield surface, whereas σ^* is submitted to an elastic-plastic variation. The strain state of the solid being ultimately the same in both cases, it will be likewise for the stress states and we shall obtain

$$\sigma + d\sigma = \sigma^* + \Delta\sigma^* \quad (A1)$$

We can then imagine a thermodynamic cycle (Fig. A1) including an actual irreversible plastic deformation (3) ($d\sigma$ variation) and a virtual elastic-plastic and, therefore, reversible deformation (4) ($\Delta\sigma^*$ variation), these strains being equal from our precedent hypo-

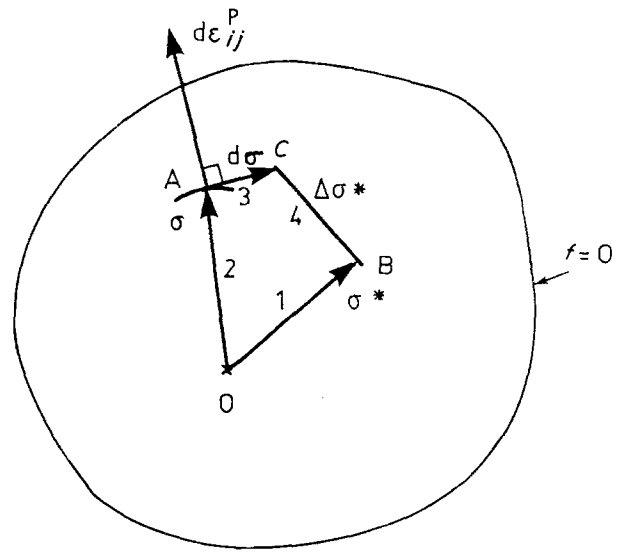


Figure A1 Carnot thermodynamic cycle in the stress space.

thesis.

$$d\epsilon_{ij3}^P = d\epsilon_{ij4}^{EP} = d\epsilon_{ij}^P = d\epsilon^P \quad (A2)$$

where E indicates elastic, P plastic, and EP elastoplastic. The work produced by this Carnot cycle is

$$dW = - \int_1 \sigma_{ij}^* d\epsilon_{ij1}^E + \int_2 \sigma_{ij} d\epsilon_{ij2}^E + \sigma_{ij} d\epsilon_{ij3}^P - \sigma_{ij}^* d\epsilon_{ij4}^{EP} \quad (A3)$$

We suppose that elastic works 1 and 2 are identical and then cancel each other to give

$$dW = (\sigma_{ij} - \sigma_{ij}^*) d\epsilon_{ij}^P \geq 0 \quad (A4)$$

Indeed, the work due to an irreversible thermodynamic cycle is ≥ 0 in accordance with the second principle of thermodynamics.

Therefore, we can infer that the work of actual stresses is higher or equal to the work due to any other tensor, the representative vector of which being on or within the yield surface and which would induce the same plastic strain. For a given deformation, actual stresses would thus have a tendency to be maximum to satisfy this maximum plastic work principle. This fact is illustrated particularly by our second stability criterion for a rolling texture (see Section 4), this criterion being, therefore, related to a concept of energy.

Appendix 2. $\langle 100 \rangle$ and $\langle 110 \rangle$ Burgers vector dislocation energy calculations

An earlier document [34] and Hasson's thesis [36] have shown that a slight disoriented flexion grain boundary around a $[001]$ axis in a face-centred cubic metal bicrystal can be assimilated to a $b = a [100]$ Burgers vector edge-dislocation wall, this Burgers vector being orthogonal to the boundary plane of the bicrystal.

Fig. A2 shows such a boundary, the disorientation of which is $\theta = 12^\circ 41'$ around $[001]$. a is the side of

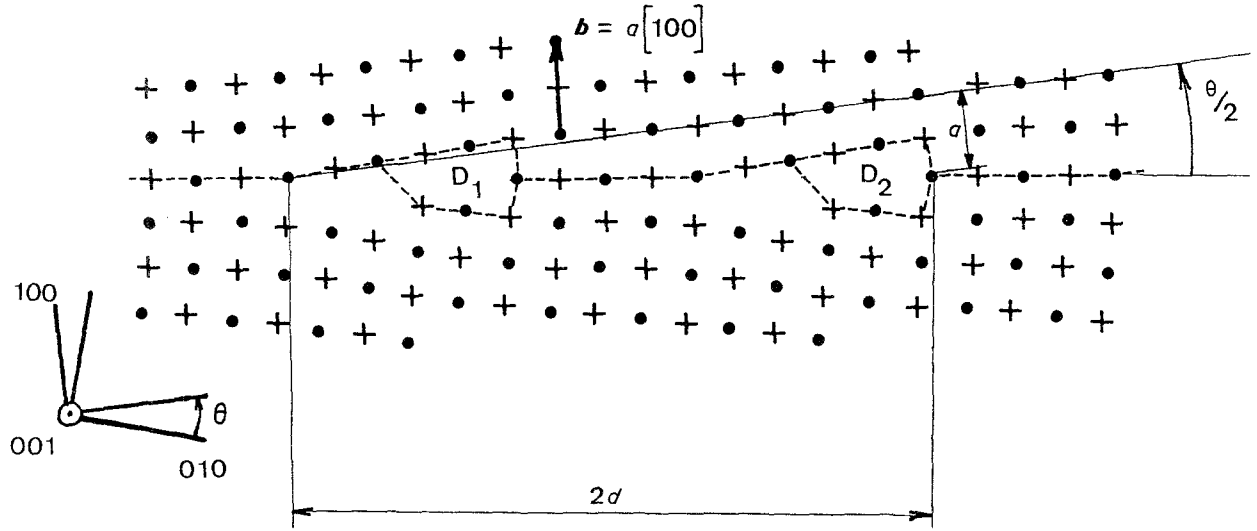


Figure A2 Slight disorientation grain-boundary structure scheme obtained by rotation $\theta = 12^\circ 41'$ around $[001]$ of two face-centred cubic crystals. The grain boundary is $[01\bar{9}]$ type.

the face-centred cubic element. In the $2d$ length, there are two dislocations D_1 and D_2 , with

$$\sin \frac{\theta}{2} \simeq \frac{\theta}{2} \simeq \frac{a}{2d} \quad (\text{A5})$$

and

$$d \simeq \frac{a}{\theta} \quad (\text{A6})$$

where d is the mean distance between two consecutive dislocations. For $\theta = 12^\circ 41' = 0.221$ rad

$$d = \frac{a}{\theta} = 4.525a \quad (\text{A7})$$

The dislocation number per unit of boundary length (1 cm) is then

$$N = \frac{1}{d} = \frac{1}{4.525a} \quad (\text{A8})$$

with a in cm. In other respects, Hasson's thesis [36] allows us to determine the flexion around $[001]$ boundary energy in an aluminium bicrystal for a given disorientation angle, θ . For $\theta = 12^\circ 41'$, we find from Fig. A3 $W = 450 \text{ erg cm}^{-2}$ at $T = 440 \text{ K}$, which is nearest to room temperature.

For a $1 \text{ cm} \times 1 \text{ cm}$ grain boundary, hence for 1 cm long dislocations, each dislocation energy will be

$$E_{100} = \frac{W}{N} = 4.525aW \quad (\text{A9})$$

with $a = 0.406 \text{ nm}$ for aluminium.

We find $E_{100} = 8.27 \times 10^{-5} \text{ erg lin.cm}^{-1}$. We can compare this $b = a[100]$ Burgers vector dislocation energy with the energy of a standard edge dislocation: $b = \frac{1}{2}a\langle 110 \rangle$ which will be calculated by the continuous medium formula

$$E_{100} = \frac{\mu b^2}{4\pi(1-\nu)} \log \frac{r_1}{r_0} \quad (\text{A10})$$

with, for aluminium, $\mu = 2.7 \times 10^{11} \text{ dyn cm}^{-2}$,

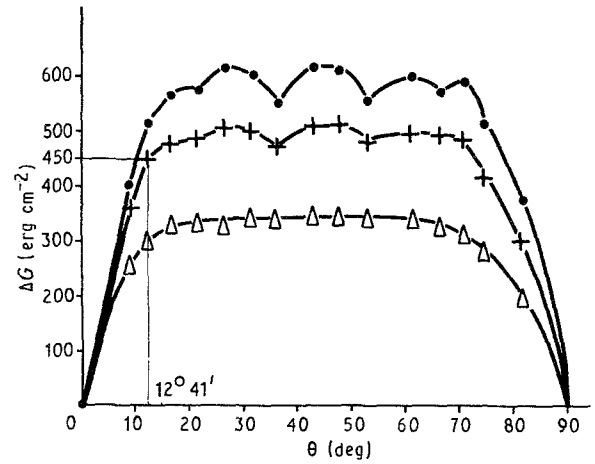


Figure A3 Influence of disorientation, θ , of a bicrystal on the free energy of the symmetrical flexion grain boundaries around $[001]$ axis at different temperatures, (from [36]). $T(K)$: (●) 0, (+) 440, (Δ) 900 ($T - T_F$).

$b = a/2^{1/2}$ and $a = 4.06 \times 10^{-8} \text{ cm}$, $\nu = 0.3$, $r_1 \simeq 10r_0$ (dislocation influence zone). We find $E_{110} = 5.82 \times 10^{-5} \text{ erg lin.cm}^{-1}$.

Thus, we discover that the $\langle 100 \rangle$ edge dislocation in aluminium has an energy not much greater (1.4 times) than that of the $\langle 110 \rangle$ standard edge dislocation and therefore the existence and stability of this $\langle 100 \rangle$ dislocation are not rendered unlikely by virtue of too high an energy.

Moreover, examinations by electron microscopy of linear defects in slight disorientation around $[100]$ flexion grain boundaries have shown that these defects could be likened to $b = a[100]$ Burgers vector edge dislocations and that these dislocations are stable and observable and are not composed of $\langle 110 \rangle$ partial standard dislocations [34].

References

1. G. SACHS, *Z. Ver. Deut. Ing.* **72** (1928) 734.
2. W. BOAS and E. SCHMID, *Z. Tech. Phys.* **12** (1931) 71.

3. G. I. TAYLOR, *J. Inst. Metals* **62** (1938) 307.
4. M. R. PICKUS and C. H. MATHEWSON, *ibid.* **64** (1939) 237.
5. F. WEVER and W. E. SCHMID, *Z. Metallkde* **22** (1930) 133.
6. R. WALTER, J. HIBBARD and MING KAO YEN, *Trans. AIME* **175** (1948) 126.
7. E. A. CALNAN and C. J. B. CLEWS, *Phil. Mag.* **41** (1950) 1085.
8. J. F. W. BISHOP and R. HILL, *ibid.* **42** (1951) 414.
9. *Idem*, *ibid.* **42** (1951) 1298.
10. F. HAESSNER, *Z. Metallkde* **54** (1963) 98.
11. G. Y. CHIN and W. L. MAMMEL, *Trans. AIME* **239** (1967) 1400.
12. I. L. DILLAMORE and W. T. ROBERTS, *Acta Metall.* **12** (1964) 281.
13. I. L. DILLAMORE, E. BUTLER and D. GREEN, *Met. Sci. J.* **2** (1968) 161.
14. I. L. DILLAMORE and H. KATOH, BISRA Open Report (1971).
15. *Idem*, *Met. Sci. J.* **8** (1974) 1.
16. HSUN HU, R. S. CLINE and S. R. GOODMAN, "Recrystallization, Grain Growth and Texture" (ASM, Metals Park, OH, 1965).
17. Y. C. LIU, *Trans. AIME* **230** (1964) 656.
18. P. R. THORNTON, T. E. MITCHELL and P. B. HIRSCH, *Phil. Mag.* **2** (1962) 1349.
19. G. WASSERMANN, *Z. Metallkde* **54** (1963) 61.
20. H. AHLBORN, J. GREWEN and G. WASSERMANN, *ibid.* **55** (1964) 598.
21. T. LEFFERS and A. GRUM-JENSEN, *Trans. AIME* **242** (1968) 314.
22. F. HAESSNER, "Recrystallization, Grain Growth and Textures" (ASM, Metals Park, OH, 1965) p. 386.
23. C. A. VERBRAAK, Thesis, Technische Hogeschool, Delft, Holland (1959).
24. E. CALNAN, *J. Inst. Met.* **84** (1955-56) 504.
25. T. L. RICHARDS and S. F. PUGH, *J. Inst. Met.* **88** (1959-1960) 399.
26. C. J. BEEVERS and R. W. K. HONEYCOMBE, *Acta Metall.* **6** (1961) 513.
27. R. J. HARTMANN and E. MACHERAUCH, *Z. Metallkde* **51** (1960) 694.
28. *Idem*, *ibid.* **52** (1961) 353.
29. M. MACLEAN and H. MYKURA, *Acta Metall.* **13** (1965) 376.
30. A. SPOLIDOR, Thesis, Paris (1983).
31. A. SPOLIDOR and C. GOUX, *C.R. Acad. Sci. Paris* **286** (1978) C-341.
32. R. C. J. GALLAGHER and Y. C. LIU, *Acta Metall.* **17** (1969) 127.
33. A. SPOLIDOR, J. RIEU and C. GOUX, *C.R. Acad. Sci. Paris* **280** (1975) 329.
34. J. LÉVY, *ibid.* **264** (1967) C-273.
35. I. L. DILLAMORE, I. R. HARRIS and R. E. SMALLMAN, *Acta Metall.* **12** (1964) 155.
36. G. HASSON, Thesis, Paris (1972).

*Received 3 September 1991
and accepted 18 March 1992*